*Journal of The Electrochemical Society*, **156** (8) G114-G119 (2009)
0013-4651/2009/156(8)/G114/6/$25.00 © The Electrochemical Society

# Structural and Dielectric Properties of Sputter-Deposited $Ba_{0.48}Sr_{0.52}TiO_3/LaNiO_3$ Artificial Superlattice Films

**Hsin-Yi Lee,[a,z] Heng-Jui Liu,[a] Yuan-Chang Liang,[b,*] Kun-Fu Wu,[c] and Chih-Hao Lee[c]**

[a]*National Synchrotron Radiation Research Center, Hsinchu Science Park, Hsinchu 30076, Taiwan*
[b]*Department of Mechanical Engineering, Chienkuo Technology University, Changhua 500, Taiwan*
[c]*Department of Engineering and System Science, National Tsing Hua University, Hsinchu 30013, Taiwan*

Artificial superlattices consisting of dielectric $Ba_{0.48}Sr_{0.52}TiO_3$ (BST) and conductive $LaNiO_3$ (LNO) were fabricated on an Nb-doped $SrTiO_3(001)$ single-crystal substrate with radio-frequency magnetron sputtering at temperatures in the range of 500–700°C. A symmetric structure with a sublayer thickness of 3 nm was deposited at varied substrate temperatures; the superlattices contained 10 periods of BST/LNO bilayers. The microstructure of these films was characterized with measurements of X-ray reflectivity and diffraction at high resolution. The formation of a superlattice structure was confirmed through the appearance of both the Bragg peaks separated by Kiessig fringes in X-ray reflectivity curves and the satellite peaks of a (002) diffraction pattern and the secondary-ion mass spectrometry profile. The clearly discernible main feature and satellite features observed in the (002) crystal truncation rod indicate the high quality of the BST/LNO artificial superlattice structure formed on a $SrTiO_3$ substrate at all temperatures of deposition. The higher the temperature of deposition, the smaller the full width at half-maximum of the in-plane rocking curve and the better the crystalline quality. These BST/LNO artificial superlattices show a dielectric constant significantly enhanced relative to the BST single layers of the same effective thickness. Both the lattice strain and the interface quality affect the dielectric properties of the BST/LNO superlattices.
[DOI: 10.1149/1.3151928]

Manuscript submitted November 20, 2008; revised manuscript received May 11, 2009. Published June 22, 2009.

Ferroelectric thin films of perovskite structure have attracted much attention because of their remarkable ferroelectric and electro-optical properties and large dielectric constant (relative permittivity).[1-4] Strain in ferroelectric thin films plays a significant role in influencing their dielectric properties, which are important for electronic applications, but the manipulation of this strain from the substrate is limited for thick films.[5,6] An artificial superlattice structure provides an alternative approach to manipulate the strain of ferroelectric thin films. Stress is artificially introduced into the heteroepitaxial superlattice films through a lattice mismatch at the interface between heterolayers. There is great interest in growing artificial superlattices of ferroelectric oxides for their ability to improve the properties of materials through structural modifications.[7-12]

Various techniques including molecular beam epitaxy (MBE) and pulse laser deposition (PLD) have been used to grow epitaxial superlattice films of complex oxides. Both these methods offer the advantage of maintaining control of stoichiometry, crystal structure, etc. For this reason, epitaxial superlattice films of complex oxides are typically prepared either by PLD or MBE at high temperatures.[11,13] Sputtering is one of the most important methods for epitaxial perovskite-oxide film deposition due to high reproducibility in the chemical composition and easy process control.[14-16] As there exists little information on superlattice films prepared with radio-frequency (rf) sputtering, the investigation of ferroelectric properties vs the strain dependence of superlattice films prepared with rf sputtering on a microscopic scale is significant for the development of materials in this class. We have fabricated several ferroelectric superlattices of perovskite-oxide structure with rf sputtering.[9,17-19] Our research has focused mostly on the correlation of dielectric properties with strain and the dependence on thickness; it is difficult to distinguish whether the variation in dielectric properties is caused by lattice distortion or increasing thickness because dielectric properties approach bulk values with increasing film thickness. To discriminate between the dielectric properties based on thickness and those based on strain dependence, we fabricated $Ba_{0.48}Sr_{0.52}TiO_3/LaNiO_3$ (BST/LNO) superlattices with varied temperatures of deposition to induce the different strain states in the films. According to measurements of X-ray reflectivity and diffraction, all these films have a periodic structure and epitaxy; a strain state that varies with deposition temperature is observable with grazing incident X-ray diffraction (XRD) patterns. In the present work, we examined the structure and dielectric properties of a BST/LNO superlattice grown on $SrTiO_3$ (STO) with rf sputtering with deposition temperatures in the range of 500–700°C. We used LNO because it has a satisfactory crystallographic compatibility for a heteroepitaxial growth of a BST layer; a lattice parameter smaller than that of BST introduces a strain through a lattice mismatch at an interface.[20-22] In this superlattice system, the dielectric properties of the superlattice film result mainly from the portion of dielectric layers, i.e., BST, because of the conductive property of the LNO material. Insulating/conductive superlattice materials of this type are therefore used for the investigation of the strain dependence of the dielectric properties of BST layers in superlattice structures.

## Experimental

The BST/LNO superlattice was grown on a conductive Nb-doped single-crystal STO(001) substrate with a triple-gun rf magnetron sputtering system and computer control of the shutter opening; we thereby precisely controlled the duration of the deposition of each layer during the deposition of a superlattice. The STO substrate was cleaned with supersonic rinsing with propanone and ethanol and subsequently heated at 650°C for 20 min in an oxygen atmosphere (2 Pa) to clean the surface. To obtain epitaxial superlattice thin films, we varied the substrate temperature and input power density systematically. We found that for a substrate temperature below 500°C, only partially crystalline or polycrystalline films were grown, whereas epitaxial superlattice thin films were obtained under conditions of substrate temperatures 500–700°C and power densities $2.5\ W/cm^2$ for BST and $1.5\ W/cm^2$ for LNO with a highly purified gas $(25\%\ O_2 + 75\%\ Ar)$ at a working pressure of 1 Pa. With these parameters, the rate of growth of a deposited film for a BST or LNO sublayer was about 2 or 1 nm/min, respectively. The deposition was interrupted for 12 s between the growths of consecutive sublayers. The superlattice contained 10 periods of BST/LNO with each 3 nm thick sublayer deposited at temperatures in the range of 500–700°C.

X-ray reflectivity measurements were performed using Cu Kα radiation in a standard Huber four-circle X-ray diffractometer operated at 50 kV and 200 mA in the X-ray Laboratory at National Synchrotron Radiation Research Center (NSRRC), Hsinchu, Taiwan. The incident light was made monochromatic with a flat

---

[*] Electrochemical Society Active Member.
[z] E-mail: hylee@nsrrc.org.tw

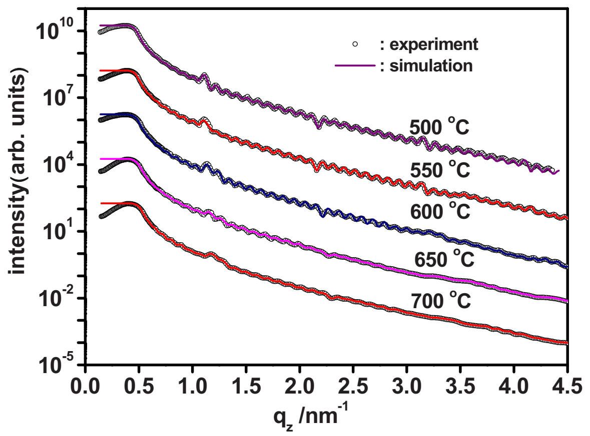

**Figure 1.** (Color online) Reflectivity curves (circles) of BST/LNO superlattice films deposited at varied substrate temperatures and their best-fit results (solid line) as a function of momentum transfer.

Ge(111) crystal; two sets of slits served to eliminate Cu $K\alpha_2$ contamination, yielding a wave-vector resolution in the scattering plane of order 0.015 nm$^{-1}$.

The superlattice structure was also characterized on measuring the crystal truncation rod (CTR) intensity with a synchrotron X-ray source; these synchrotron experiments were performed at wiggler beamline BL-17B1 of NSRRC. Incident X-rays were focused vertically with a mirror and made monochromatic to an energy of 8 keV with a Si(111) double-crystal monochromator; the sagittal bend of the second crystal focused the X-rays in the horizontal direction. With two pairs of slits between the sample and the detector, the typical scattering vector resolution in the vertical scattering plane was set to $\sim 1 \times 10^{-3}$ nm$^{-1}$ in these experiments.

The composition depth profile was also examined with a secondary-ion mass spectrometer (SIMS) and an oxygen-ion source. The surface morphology of the films was obtained with an atomic force microscope (AFM). An AFM image was obtained on an instrument (Park Scientific, Auto Probe M5) operated under ambient conditions in a contact mode using a silicon tip (with a diameter of 15 nm). Various areas ($2 \times 2$ μm) of the surfaces were scanned at a rate of 1.2 Hz. A computer program automatically calculated the root-mean-square surface roughness. For measurements of electrical properties, Pt top electrodes were sputtered onto the surface of the superlattice films near 25°C. The dielectric properties of the superlattices were measured near 25°C with a low frequency impedance analyzer (HP 4192A, frequency of 10 kHz).

## Results and Discussion

Figure 1 presents the reflectivity curves of BST/LNO superlattice films deposited at varied substrate temperatures and their best-fit results. For each curve, the diffuse scattering was measured and subtracted, so that the data points represent only the specular component. As the real part of the refraction index is slightly smaller than unity for all these materials, total external reflection occurs for $\theta_i \leqq \theta_c$, in which $\theta_c$ is the critical angle of the total reflection and $\theta_i$ is the incident angle of the X-ray beam. At a small incident angle, the footprint of the beam is typically larger than the sample surface, and only part of the light becomes reflected; the increased reflectivity intensity is thus due to the surface effect when the incident angle is less than $\theta_c$. The presence of clear oscillations indicates that both the surface and the interface correlate well with each other and are smooth enough to produce the oscillations. Both the superlattice peaks and the Kiessig oscillations, which were well pronounced, reveal the presence of a well-ordered layer structure of a superlattice, providing evidence for a vertically periodic modulation of the composition.

To acquire the physical parameters of the superlattice, we based the simulation of the specular reflectivity on the recursive formalism of Parratt.[23] We fitted the reflectivity data with the Bede$_{\text{refs}}$ Mercury code[24] to determine the physical parameters of the superlattice, including roughness, thickness, and density. This program calculates the reflectivity of the material using the dynamic Fresnel equations for multilayer reflectivity, taking into account the absorption, instrumental resolution, interface roughness and abruptness, and sample curvature. According to the best-fit results in Table I, the densities of the BST and LNO sublayers are slightly less than their bulk values; this condition likely reflects an increased density of defects that inevitably occur during the deposition of a thin film at a high temperature.[9,25-27] We also found that the sublayer thickness decreased with increasing substrate temperature, indicating a rate of growth inversely proportional to temperature; such a decreased rate is attributed to a smaller sticking coefficient and a greater mobility of atoms adsorbed on the surface that become more readily resputtered away on ion bombardment during deposition at a higher temperature.[28,29] The reflectivity curve shows that the lower the deposition temperature, the more clearly present the superlattice peaks and the Kiessig fringes. Hence, the lower the deposition temperature, the smoother the surface and the less the interface roughness. The fitted result shows not only that the surface and interface roughness increased with increasing temperature of deposition but also that the interface roughness increased considerably for a substrate temperature of deposition ≧650°C.

To verify the vertically periodic modulation obtained from the X-ray reflectivity, we examined the vertical composition profile of the superlattices with a SIMS. A SIMS depth profile of the BST/LNO superlattice sample deposited at 600°C is shown in Fig. 2. The variations in the signals of Ba, Sr, Ti, La, and Ni are consistent with the designed period of 10 cycles of a BST/LNO superlattice. The modulation length ($\Lambda$) obtained from the SIMS depth profile is ~61 nm, which is satisfactorily consistent with the fitted result of the reflectivity curve shown in Table I, i.e., $\Lambda = (t_{\text{BST}} + t_{\text{LNO}}) \times 10 = (3.06 + 3.02) \times 10 = 60.8$ nm. This result clearly demonstrates the self-consistency of this analysis of X-ray reflectivity.

**Table I. Parameters obtained from the best-fit results of reflectivity curves of BST/LNO superlattice films deposited on an Nb-doped STO substrate with varied temperatures of deposition. The surface roughness determined from AFM measurements is listed in the last column for comparison. The relative standard deviations of the fitted data are for thickness ≦2%, density ≦2%, and roughness ≦6%. The thickness of the $SrTiO_3$ substrate is set as infinite and the bulk density is 5.118 g/cm$^3$. The bulk density of BST is 6.123 g/cm$^3$, and that of LNO is 7.086 g/cm$^3$.**

| Deposition temperature (°C) | Fitted thickness (nm) | | Fitted density (g cm$^{-3}$) | | Fitted roughness (nm) | | | AFM (nm) |
|---|---|---|---|---|---|---|---|---|
| | $t_{\text{LNO}}$ | $t_{\text{BST}}$ | $\rho_{\text{LNO}}$ | $\rho_{\text{BST}}$ | $\sigma_{\text{LNO/sub}}$ | $\sigma_{\text{interface}}$ | $\sigma_{\text{surface}}$ | $\sigma_{\text{surface}}$ |
| 500 | 3.12 | 3.15 | 6.805 | 6.113 | 0.25 | 0.46 | 0.66 | 0.61 |
| 550 | 3.11 | 3.08 | 6.944 | 6.061 | 0.27 | 0.48 | 0.67 | 0.59 |
| 600 | 3.06 | 3.02 | 6.944 | 5.98 | 0.29 | 0.49 | 0.68 | 0.66 |
| 650 | 3.01 | 2.98 | 6.805 | 6.113 | 0.28 | 0.82 | 0.70 | 0.68 |
| 700 | 2.89 | 2.92 | 6.804 | 6.114 | 0.27 | 0.84 | 0.74 | 0.71 |

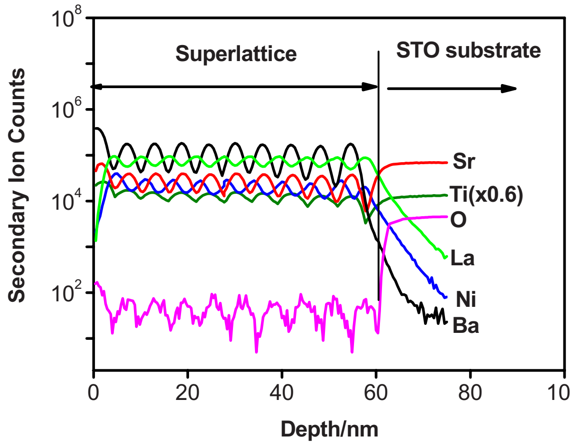

**Figure 2.** (Color online) SIMS depth profile of a BST/LNO superlattice deposited at 600°C.

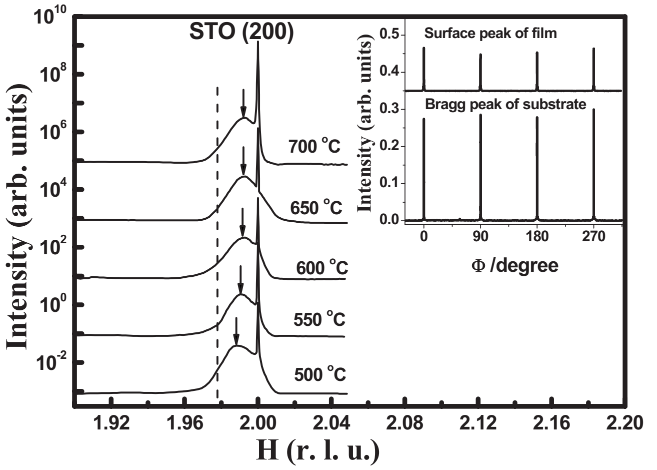

**Figure 4.** X-ray intensity of a set of radial scans along the (200) in-plane Bragg peak of BST/LNO superlattice films deposited at varied substrate temperatures. An arrow marks the position of the superlattice main peak, and a dashed line presents the position of the mean value of the superlattice. The inset shows an azimuthal scan (Φ scan) of the surface peak and the substrate Bragg peak for a superlattice film deposited at 550°C.

To confirm the X-ray reflectivity results, we examined the surface roughness of the deposited films with an AFM. For comparison, the surface roughness evaluated from AFM images is listed in Table I. The results obtained from these two methods agree satisfactorily.

Figure 3 shows the variation with the substrate temperature of CTR spectra along the direction [00$L$] of BST/LNO superlattice films. Values of $H$, $K$, and $L$ given in this paper are expressed in reciprocal lattice units referred to the STO lattice parameter, 0.3905 nm at 25°C. The intense and sharp feature centered at $L = 2$ is the STO(002) Bragg reflection from the substrate, as shown in Fig. 3. The main feature (marked with arrows in Fig. 3) and the satellite peaks that are accompanied with clearly discernible Pendellösung fringes on both sides of the main peak indicate the high quality of the BST/LNO artificial superlattice structure formed on the STO substrate with rf magnetron sputtering at all deposition temperatures.

Using grazing incidence scattering geometry, we examined the epitaxial relationship also from in-plane X-ray scans on these superlattice films. The distribution of the in-plane X-ray intensity of the radial scans from superlattice films with varied deposition temperatures is shown in Fig. 4 The scan was performed in the vicinity of the STO(200) Bragg peak; the angle of incidence was fixed at 0.3° with respect to the sample surface during the measurement. A broad feature coexists with a sharp Bragg peak, which originates from the substrate. This broad feature, indicated by arrows in Fig. 4, is ascribed to the Bragg peak of the deposited layer, which is confirmed by the variation in relative intensity between the two peaks as a function of angle of incidence. Furthermore, azimuthal scans of a superlattice film deposited at 550°C in the vicinity of a surface peak and the substrate Bragg peak, as shown in the inset of Fig. 4, clearly exhibit a fourfold symmetry with the same orientation. No other feature was observed in the intervals between the four peaks, indicating a perfect alignment of the *a* and *b* axes of BST and LNO unit cells along those of the STO substrate. These results provide firm evidence for a strong epitaxial layer deposited on the substrate. Figure 5 shows that the full width at half-maximum (fwhm) of these in-plane rocking curves decreases with increasing temperature of deposition. The narrower the fwhm of this rocking curve is, the better known the crystalline quality is.

The BST and LNO films are describable as having a pseudocubic structure, with bulk lattice parameters of 0.4018 nm for BST and 0.3887 nm for LNO. In this superlattice system, the BST sublayer is in a biaxially compressive state, whereas the LNO sublayer is in a biaxially tensile state.[18] These heteroepitaxial sublayers are hence characterized by either being strongly strained or containing many misfit dislocations with a modulation length larger than a critical

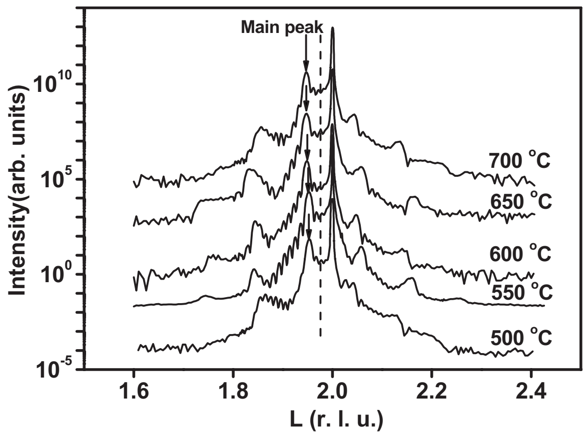

**Figure 3.** Intensity distribution of a (002) CTR spectrum of BST/LNO superlattice films deposited at varied substrate temperatures. An arrow marks the position of the superlattice main peak, and a dashed line presents the position of the mean value of the superlattice.

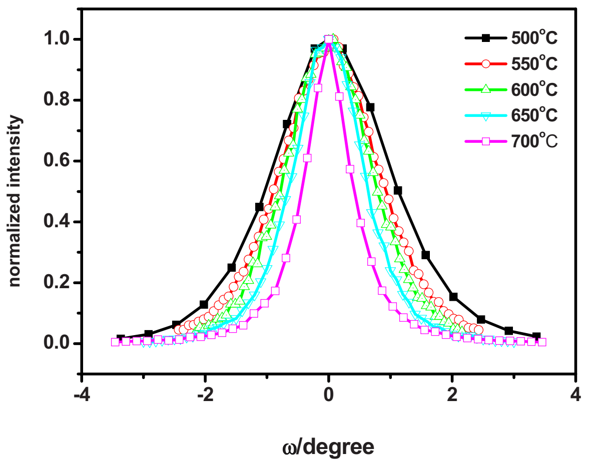

**Figure 5.** (Color online) Rocking curves of the in-plane (200) main peak of BST/LNO superlattice films deposited at varied temperatures.

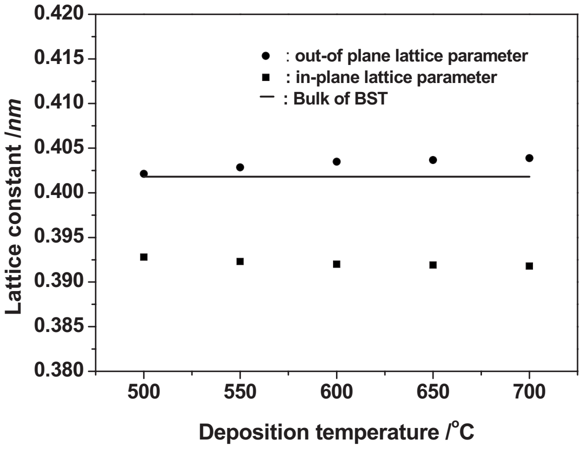

**Figure 6.** Measured mean out-of-plane (*c*-axis) and in-plane (*a*-axis) lattice parameters of BST/LNO superlattice films with varied deposition temperatures.

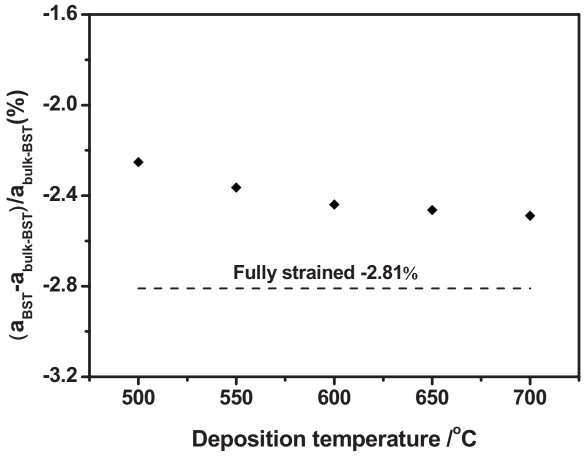

**Figure 7.** In-plane compressive strain of a BST layer as a function of deposition temperature.

value. The critical thickness for the misfit dislocations was roughly estimated according to a model proposed by Matthews.[9,30] We calculated the critical thickness of the BST/LNO superlattices to be ~15 nm. The designed modulation length of prepared superlattices (6 nm) is within the theoretically estimated lengths.

The expected mean lattice parameter ($a_{\text{mean}}$) of a superlattice film is calculated according to

$$\frac{2}{a_{\text{mean}}} = \frac{1}{a_{\text{bulk BST}}} + \frac{1}{a_{\text{bulk LNO}}} \qquad [1]$$

With the bulk values of BST and LNO inserted therein, we thus calculated $a_{\text{mean}} = 0.39514$ nm, larger than 0.3905 nm, which is characteristic of the single-crystal substrate STO, and indicated as a dashed line in Fig. 3. The position of the main peak (zeroth-order peak) in the (002) CTR spectra of the superlattices, as shown in Fig. 3, is determined by the average *c*-axis length of the superlattice.[8,9] The *L* index of the main peak (marked with arrows in Fig. 3) of the BST/LNO superlattice is smaller than the weighted mean value (indicated as a dashed line in Fig. 3) from unstrained BST and LNO films, i.e., $L = 1.9764$. The main lattice parameter *c* of the BST/LNO superlattices is larger than the weighted mean of the lattice parameter *c* of unstrained BST and LNO films, indicating an elongation of the average *c*-axis lattice of the superlattice along $[00L]$ through the heteroepitaxial strain in the superlattice structure, i.e., enhancing the tetragonality of BST sublayers in the superlattice structure. Moreover, the position of the main peak of the BST/LNO superlattices shifts slightly to a decreasing *L* index with increasing temperature of deposition. This condition indicates that the superlattice films become subject to the increased tensile stress along the *c* axis (plane normal direction) on increasing the temperature of deposition. In contrast, the position of the in-plane main peak for all superlattice films (marked with arrows in Fig. 4) is larger than the mean value of the superlattice (indicated as a dashed line in Fig. 4) and approaches the STO substrate Bragg peak with an increasing temperature of deposition. Increasing the temperature of deposition thus subjects the superlattice films to increased compressive stress parallel to the surface plane. Superlattice films deposited at a higher temperature thus have an enhanced tetragonality of BST sublayers in a superlattice structure relative to films deposited at a lower temperature.

The in-plane lattice parameter of BST can be determined directly from the in-plane (200) reflection shown in Fig. 4.[9,31] Although the *c*-axis parameter of a BST layer cannot be determined directly with the (002) CTR spectra shown in Fig. 3, we can still evaluate the parameter through the elastic relationship between the strain normal to the interface in the cubic structure.[32-34] Figure 6 shows the measured mean out-of-plane (*c*-axis) and in-plane (*a*-axis) lattice parameters of superlattices with varied deposition temperatures. The mean *c*-axis parameter of the superlattice increases slightly with increasing temperature of deposition, whereas the *a*-axis parameter decreases. An elongation of the *c* axis of the BST lattice by the heteroepitaxial strain in the superlattice clearly occurs. Under the conditions of biaxial strain, which apply for a BST epitaxial layer on $(00L)$, the in-plane nonvanishing compressive strain component is defined as $(a_{\text{BST}} - a_{\text{bulk BST}})/a_{\text{bulk BST}}$, in which $a_{\text{BST}}$ is the lattice parameter of the strained BST layer that is obtainable from the measured in-plane lattice parameter of the superlattices and $a_{\text{bulk BST}}$ is the bulk lattice parameter of unstrained BST. The evaluated strain of BST layers in the superlattice is shown in Fig. 7. An in-plane lattice parameter of 0.3905 nm is necessary for the fully strained pseudomorphic growth of BST/LNO superlattices on a STO substrate. The critical thickness of a superlattice depends on the elastic properties of the constituent sublayers, but there is still a critical thickness for a superlattice having a modulation length with thickness not exceeding its critical value.[17,18,31] The lattice mismatch between the in-plane lattice parameter of the least strained BST–LNO bilayer, which is 0.3945 nm, and that of the STO substrate is 1.02%, which allows pseudomorphic growth for only a few nanometers.[9] The superlattices of BST/LNO with a total thickness of ~60 nm exceed the critical value to generate misfit dislocations from a prediction of Matthews' law.[9,30] The fully strained pseudomorphic growth of each layer is thus not proceeding in the superlattice during deposition, even though the thickness of individual BST and LNO layers is less than the critical thickness.[7,9,18] The BST/LNO superlattice films reveal a partial strain relaxation and not a fully strained state for all temperatures of deposition, as shown in Fig. 7. Deposition at a higher temperature also clearly results in a larger in-plane compressive strain of the BST sublayers in the superlattice.

In the BST/LNO superlattice system, the dielectric properties of the superlattice film result mainly from the portion of the dielectric layer, i.e., BST layers, because of the conductive property of the LNO material. Figure 8 depicts the dielectric constant and the value of dielectric loss, tan δ, measured at 10 kHz, of the BST layer evaluated from the measured capacitance without taking the influence of the interface structure into consideration. The surface of the free-energy minimum in a strained system is not atomically smooth but three-dimensional growths in form. Hence, the presence of strain forces the close-to-equilibrium surface of the strained epilayer toward a three-dimensional island growth.[35] Moreover, the conformal structure was found in the prepared superlattices from nonspecular scattering herein. The interface roughness of the BST/LNO interface is attributed to the conformal roughness.[36] Moreover, no Bragg reflections resulted from the interface compound due to atomic inter-

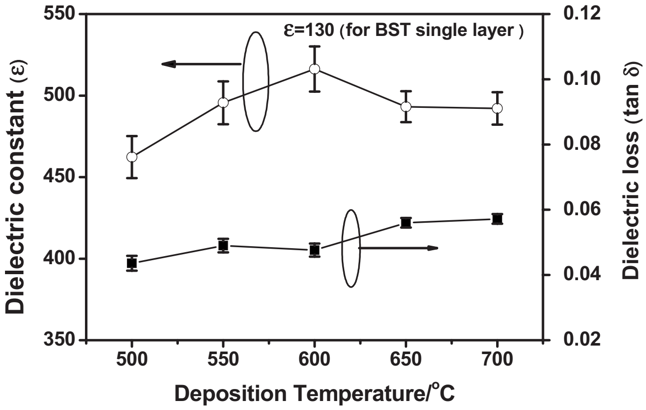

**Figure 8.** Dielectric constant ($\varepsilon$) and value of dielectric loss (tan δ) of a BST layer measured at 10 kHz as a function of deposition temperature. For a single-layer film of BST 30 nm thick, $\varepsilon_f = 130$.

diffusion between the BST and the LNO that was observed in the in- and out-of-plane synchrotron XRD patterns. Both facts support that the interface roughness might not be caused by the interdiffusion between the constituent layers. Because an interfacial roughness resulting from the lattice strain is formed between BST and LNO layers, the effective thickness of the BST layers must exclude the interfacial portion, and the dielectric contribution from the rough interface should also be taken into account separately. Thus, the capacitance of the superlattice can be treated to a series capacitance of the effective BST and the interface,[9,37,38] i.e., $A/C_{\text{meas}} = A/C_{\text{BST}} + A/C_i$, where $A$ is the area of the top electrode, $C_{\text{meas}}$ is the measured capacitance, $C_{\text{BST}}$ is the capacitance of the effective BST layer, and $C_i$ is the capacitance of the interface. The dielectric constant of the effective BST layer, $\varepsilon_{\text{BST}}$, is then obtained from the following equation

$$A/NC_{\text{meas}} = (d_{\text{BST}} - d_i)/\varepsilon_{\text{BST}} + d_i/\varepsilon_i \tag{2}$$

where $N$ is the number of BST sublayers, $d_{\text{BST}}$ is the thickness of the BST sublayer, $d_i$ is the thickness of the interface, which is estimated from the interface roughness, and $\varepsilon_i$ is the dielectric constant of the interface. All the thickness data can be obtained from the fitted result of X-ray reflectivity. To estimate the dielectric constant of the effective BST layer, we prepared one extra sample with 12 periods of BST/LNO superlattice deposited at 600°C. The dielectric constant of the effective BST layer obtained from the above equation is ($\varepsilon_{\text{BST}} \sim 436$) three times larger than the 30 nm thick single BST layer film ($\varepsilon \sim 130$) prepared under the same sputtering condition at 600°C. This result clearly indicates that the strained BST layers of the superlattice film show the significant dielectric enhancement relative to the single BST layer films. Furthermore, these large dielectric constants can be maintained at a high frequency of 400 kHz, as shown in Fig. 9. The dielectric constant of BST/LNO superlattices decreased gradually with the increasing applied frequency, whereas the dielectric constant of the 30 nm thick single BST layer film is maintained nearly constant. It is considered that the dielectric dipole moment consists of the oriented, ionic, and electric polarizations above the frequency of 1 kHz.[39] In the superlattices, the dielectric constants decrease rapidly below the applied frequency of 1 kHz. This may be due to the space charge and dipolar polarizations at the interfaces between BST and LNO layers. Space charge and dipolar polarizations are relaxation processes and are strongly temperature dependent; ionic and electric polarizations are resonance processes and sensibly temperature independent. Tabata et al.[40] reported that the dielectric enhancement in the $BaTiO_3/SrTiO_3$ superlattice system is related to the soft-mode coupling with the expansion of the average out-of-plane ($c$-axis) lattice parameter. Therefore, there is a strain (or a lattice distortion) that causes softening of the optical phonons; the dielectric constant is expected to increase greatly.[41-43] Previous authors have shown that a large dielectric constant was obtainable at a degree of strain modified on inserting a thin interlayer.[42,43] As illustrated in Fig. 7, the BST sublayers in the superlattices experience a larger compressive strain (or a larger lattice distortion) that greatly elongates their unit cells along the electric field in the parallel-plate capacitor structure relative to the single BST epilayers of the same effective thickness that have an in-plane strain of −0.21% only. This result clearly reveals that an effective strain manipulation of BST sublayers in a superlattice structure by alternating insertion of LNO sublayers greatly enhances the dielectric constant of the BST sublayers. In a parallel capacitor structure, the dielectric constant of ferroelectric thin films increases with increasing in-plane compressive stress.[44,45] Thus, increasing the temperature of deposition of BST/LNO superlattices results in an increased in-plane compressive strain in the BST sublayers, further enhancing the tetragonality of BST unit cells; this effect results in an increased dielectric constant of BST/LNO superlattices with increasing temperature of deposition. The dielectric property results (Fig. 8) show that the dielectric constant increases with increasing temperature of deposition except for films deposited at 650 and 700°C. The fitted result of the X-ray reflectivity curve shows that the interfacial roughness for superlattice films deposited at 650 and 700°C is much larger than the others. Although these superlattice films have greater tensile stress along the $c$ axis and superior crystalline quality, they also have narrower effective BST layers. The slightly decreased dielectric constant of superlattice films deposited at 650 and 700°C might be attributed to the poor interface structure of BST/LNO.

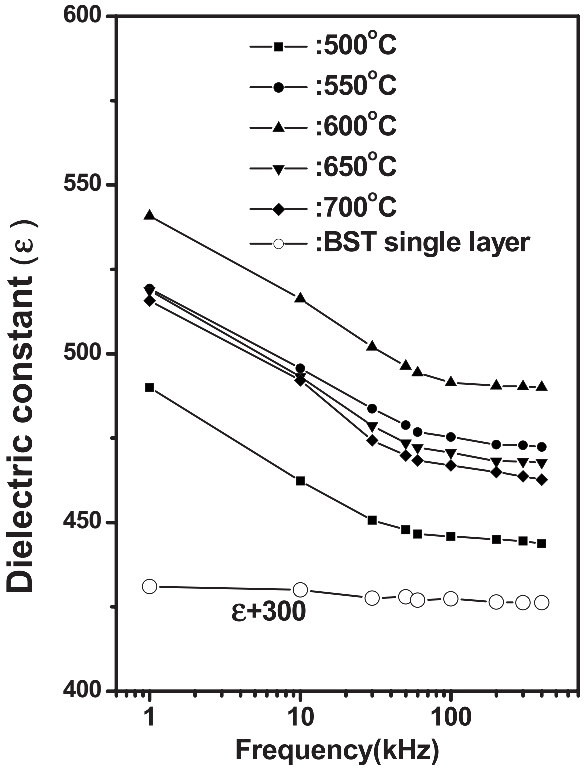

**Figure 9.** Dielectric constant of a BST layer as a function of measured frequency for BST/LNO superlattice films deposited at various substrate temperatures.

Figure 10 shows the current-density–voltage ($J$-$V$) curve of the BST/LNO superlattice films with varied deposition temperatures and a single BST layer film. It shows high current densities of leakage in this superlattice system for all temperatures of deposition compared with the 30 nm thick single BST layer film. Indeed, in an

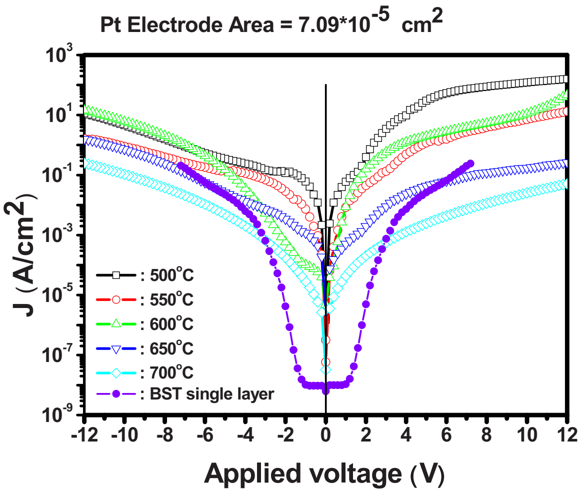

**Figure 10.** (Color online) *J-V* curves of BST/LNO superlattice films with varied deposition temperatures.

insulating/conductive superlattice system, i.e., the BST/LNO superlattice, there is a metallic layer in between, which leads to an increase in leakage current. An asymmetry feature of *J-V* curves may be due to the different Schottky barrier heights of the top and bottom electrodes or the different amount of interface defects at both sides.[46,47] The leakage current densities decreased with the increasing temperature of deposition, and it seems consistent with the tendency of the crystalline quality of the films. The higher the temperature of deposition, the smaller the fwhm of the in-plane rocking curve and the smaller the mosaic structure of the film to reduce the probability of leakage from the top electrode to the bottom electrode.

## Conclusion

BST/LNO superlattice structures, well defined and of great crystalline quality, were fabricated on a Nb-doped STO substrate through rf magnetron sputtering at temperatures in the range of 500–700°C. With X-ray reflectivity and diffraction techniques, we characterized the structure of the buried interfaces and the surface morphology of these films. Azimuthal scans of a superlattice film in the vicinity of a surface peak and the substrate Bragg peak that clearly exhibit a fourfold symmetry with the same orientation provide firm evidence for an epitaxial relationship between the film and the substrate. The fitted result from X-ray reflectivity curves shows that the densities of the BST and LNO sublayers are slightly less than their bulk values. X-ray measurements show that these superlattice films become subject to greater tensile stress along the *c* axis, increased compressive stress parallel to the surface plane, and increased crystalline quality with increasing temperature of deposition, but the superlattices also acquire a rougher interface for a temperature of deposition $\geqq$650°C. The BST/LNO superlattices show an enhanced tetragonality of BST unit cells with increasing temperature of deposition, resulting also in an increased dielectric constant, but superlattice films deposited at 650 and 700°C also have a large interface roughness that decreases the dielectric constant and increases the dielectric loss. These results demonstrate that both strain and interface state might influence the dielectric properties of the BST/LNO artificial superlattices.

## Acknowledgment

National Science Council of Taiwan provided support under contract no. NSC 96-2216-E-213-001.

*Chienkuo Technology University assisted in meeting the publication costs of this article.*

## References

1. J. F. Scott and C. A. Paz de Araujo, *Science*, **246**, 1400 (1989).
2. M. Sayer and K. Sreenivas, *Science*, **247**, 1056 (1990).
3. Q. X. Jia, L. H. Chang, and W. A. Anderson, *J. Mater. Res.*, **9**, 2561 (1994).
4. Y. A. Boikov, Z. G. Ivanov, A. N. Kiselev, E. Olsson, and T. Claeson, *J. Appl. Phys.*, **78**, 4591 (1995).
5. C. L. Canedy, H. Li, S. P. Alpay, L. S. Riba, A. L. Roytburd, and R. Ramesh, *Appl. Phys. Lett.*, **77**, 1695 (2000).
6. W. J. Kim, W. Chang, S. B. Qadri, J. M. Pond, S. W. Kirchoefer, D. B. Chrisey, and J. S. Horwitz, *Appl. Phys. Lett.*, **76**, 1185 (2000).
7. J. Kim, Y. Kim, Y. S. Kim, J. Lee, L. Kim, and D. Jung, *Appl. Phys. Lett.*, **80**, 3581 (2002).
8. Z. Wang and S. Oda, *J. Electrochem. Soc.*, **147**, 4615 (2000).
9. Y. C. Liang, T. B. Wu, H. Y. Lee, and Y. W. Hsieh, *J. Appl. Phys.*, **96**, 584 (2004).
10. T. Shimuta, O. Nakagawara, T. Makino, S. Arai, H. Tabata, and T. Kawai, *J. Appl. Phys.*, **91**, 2290 (2002).
11. J. C. Jiang, X. Q. Pan, W. Tian, C. D. Theis, and D. G. Schlom, *Appl. Phys. Lett.*, **74**, 2851 (1999).
12. T. Tsurumi, T. Harigai, D. Tanaka, S. Nam, and H. Kakemot, *Appl. Phys. Lett.*, **85**, 5016 (2004).
13. M. Lippmaa, N. Nakagawa, M. Kawasaki, S. Ohashi, and H. Koinuma, *Appl. Phys. Lett.*, **76**, 2439 (2000).
14. S. O. Park, C. S. Huang, H. Cho, C. S. Kang, H. Kang, S. I. Lee, and M. Y. Lee, *Jpn. J. Appl. Phys., Part 1*, **35**, 1548 (1996).
15. Y. C. Liang and Y. C. Liang, *J. Cryst. Growth*, **285**, 345 (2005).
16. M. Matsuoka, K. Hoshino, and K. Ono, *J. Appl. Phys.*, **76**, 1768 (1994).
17. H. Y. Lee, C. H. Hsu, Y. W. Hsieh, Y. H. Chen, Y. C. Liang, T. B. Wu, and L. J. Chou, *Mater. Chem. Phys.*, **92**, 585 (2005).
18. Y. C. Liang, H. Y. Lee, H. J. Liu, K. F. Wu, T. B. Wu, and C. H. Lee, *J. Electrochem. Soc.*, **152**, F129 (2005).
19. H. N. Tsai, Y. C. Liang, and H. Y. Lee, *J. Cryst. Growth*, **284**, 65 (2005).
20. M. S. Chen, T. B. Wu, and J. M. Wu, *Appl. Phys. Lett.*, **68**, 1430 (1996).
21. C. Guerrero, F. Sánchez, C. Ferrater, J. Roldán, M. V. Garciá, and M. Varela, *Appl. Surf. Sci.*, **168**, 219 (2000).
22. P. Chen, S. Y. Xu, W. Z. Zhou, C. K. Ong, and D. F. Cui, *J. Appl. Phys.*, **85**, 3000 (1999).
23. L. G. Parratt, *Phys. Rev.*, **95**, 359 (1954).
24. D. K. Bowen and B. K. Tanner, *Nanotechnology*, **4**, 175 (1993).
25. H. Y. Lee and T. B. Wu, *J. Mater. Res.*, **12**, 3165 (1997).
26. H. Chen and S. M. Heald, *J. Appl. Phys.*, **66**, 1793 (1989).
27. M. Sugawara, M. Kondo, S. Yamazaki, and K. Nakajima, *Appl. Phys. Lett.*, **52**, 742 (1988).
28. J. E. Mahan, *Physical Vapor Deposition of Thin Films*, p. 269, John Wiley & Sons, New York (2000).
29. H. Y. Lee, T. W. Huang, C. H. Lee, and Y. W. Hsieh, *J. Appl. Crystallogr.*, **41**, 356 (2008).
30. J. W. Matthews and A. E. Blakeslee, *J. Cryst. Growth*, **27**, 118 (1974).
31. U. Pietsch, H. Metzger, S. Rugel, B. Jenichen, and I. K. Robinson, *J. Appl. Phys.*, **74**, 2381 (1993).
32. E. D. Specht, H. M. Christen, D. P. Norton, and L. A. Boatner, *Phys. Rev. Lett.* **80**, 4317 (1998).
33. H. H. Lee, M. S. Yi, H. W. Jang, Y. T. Moon, S. J. Park, D. Y. Noh, M. Tang, and K. S. Liang, *Appl. Phys. Lett.*, **81**, 5120 (2002).
34. D. Fuchs, M. Adam, P. Schweiss, and R. Schneider, *J. Appl. Phys.*, **91**, 5288 (2002).
35. P. R. Berger, K. Chang, P. Bhattacharya, and J. Singh, *Appl. Phys. Lett.*, **53**, 684 (1988).
36. Y. C. Liang, T. B. Wu, H. Y. Lee, and H. J. Liu, *Thin Solid Films*, **469–470**, 500 (2004).
37. J. C. Shin, J. Park, C. S. Hwang, and H. J. Kim, *J. Appl. Phys.*, **86**, 506 (1999).
38. C. Basceri, S. K. Streiffer, A. I. Kingon, and R. Waser, *J. Appl. Phys.*, **82**, 2497 (1997).
39. H. Tabata, H. Tanaka, T. Kawai, and M. Okuyama, *Jpn. J. Appl. Phys., Part 1*, **34**, 544 (1995).
40. H. Tabata, H. Tanaka, and T. Kawai, *Appl. Phys. Lett.*, **65**, 1970 (1994).
41. L. Kim, D. Jung, J. Kim, Y. S. Kim, and J. Lee, *Appl. Phys. Lett.*, **82**, 2118 (2003).
42. N. A. Pertsev, A. G. Zembilgotov, and A. K. Tagantsev, *Phys. Rev. Lett.*, **80**, 1988 (1998).
43. B. H. Park, E. J. Peterson, Q. X. Jia, J. Lee, X. Zeng, W. Si, and X. X. Xi, *Appl. Phys. Lett.*, **78**, 533 (2001).
44. S. Hyun and K. Char, *Appl. Phys. Lett.*, **79**, 254 (2001).
45. A. R. James and X. X. Xi, *J. Appl. Phys.*, **92**, 6149 (2002).
46. K. Numata, *Thin Solid Films*, **515**, 2635 (2006).
47. J. Wang, T. Zhang, J. Xiang, and B. Zhang, *Mater. Chem. Phys.*, **108**, 445 (2008).